Journal of Materials Chemistry B

ROYAL SOCIETY OF CHEMISTRY

PAPER

View Article Online
View Journal

Cite this: DOI: 10.1039/d5tb01061f

Silica substituted carbonate apatite: synthesis and analytical challenges†

Michael Anenburg, *[a] Jeff Chen,‡[b] Michael G. Gardiner, [c] Jan C. M. de Hoog,[d] Madeleine C. S. Humphreys, *[e] Owen P. Missen,[f] Stuart J. Mills[g] and Božana Pašić [a]

We use a high temperature experiment to demonstrate a coupled substitution mechanism for carbonate and silica in apatite, namely $2PO_4^{3-} \rightarrow SiO_4^{4-} + CO_3^{2-}$, with carbonate substituting for phosphate (type-B substitution). The carbonate anion group occupies a crystallographically distinct site as one of two side faces of a now vacant T site phosphate tetrahedron, and an oxygen site vacancy is formed. In our experiment, apatite is synthesised using a high-pressure carbonate flux method, resulting in large crystals amenable to a range of analytical techniques which are otherwise not feasible on the more commonly synthesised nanoscale material. The apatite is analysed with wavelength dispersive spectrometry (WDS) using an electron probe microanalyser (EPMA), secondary ion mass spectrometry (SIMS), Fourier-transform infrared spectroscopy (FTIR) using both transmission and attenuated total reflectance (ATR) techniques, and single crystal X-ray diffraction (SCXRD). There is no agreement on total carbonate contents between the analytical methods with EPMA-WDS and FTIR-ATR indicating ~5 wt% CO_2, SIMS suggesting roughly 2.6 wt% CO_2, and SCXRD unable to conclusively support one or the other. Both estimates are sufficient to account for phosphate substitution by type-B carbonate and orthosilicate (SiO_4^{4-}), but the higher 5 wt% estimate raises the possibility of additional carbonate hosted in the X channel site as type-A carbonate. The bioactivity of this type of substitution relative to other vectors (such as Na–Si) is currently unknown and requires further research. As our apatite was synthesised under geologically reasonable conditions, it also raises the possibility that this substitution is present in CO_2-rich environments in the deep Earth, such as carbonic hydrothermal fluids and carbonatite magma systems, from the mantle to the crust.

Received 5th May 2025,
Accepted 8th July 2025

DOI: 10.1039/d5tb01061f

rsc.li/materials-b

Introduction

Apatite, nominally $Ca_5(PO_4)_3(F,OH,Cl)$, is a common material in both inorganic and organic natural systems. Apatite has a crystal structure that allows for abundant substitutions and inclusion of impurities or minor elements.[1] Compounds of the apatite supergroup have the general chemical formula $M_5(TO_4)_3X$, where M is a large metal cation, T is a small cation in tetrahedral coordination, and X is an anion.[2] Apatite *sensu stricto* contains Ca and P on the M and T sites, respectively. The anion site often contains fluoride, chloride, or hydroxide anions, leading to the formula $Ca_5(PO_4)_3(F,OH,Cl)$. Two of the most common substitutions in apatite are silica in the T site, and carbonate in either the T or X sites.[3] Carbonate in the X site is designated as type-A, whereas carbonate in the T site is designated as type-B.[4] These two types consist of subtypes (B1, B2, A1, A2, *etc.*) that represent variable symmetry and orientation of the carbonate group within each of those structural sites.[5,6]

Hydroxyapatite—apatite with predominantly OH^- in the anion X site—is the major component of natural bone and teeth, and its ease of manufacture led to synthetic apatite being a common material for various medical applications, such as bone and dental implants. However, pure hydroxyapatite has low reactivity and bone integration is rather sluggish.[1,7] Silica-substituted hydroxyapatite has been demonstrated to have higher bioactivity.[1,7–17] Similarly, carbonate substitution influences

[a] Research School of Earth Sciences, Australian National University, Canberra ACT 2600, Australia. E-mail: michael.anenburg@anu.edu.au
[b] Centre for Advanced Microscopy, Australian National University, Canberra ACT 2600, Australia
[c] Research School of Chemistry, Australian National University, Canberra ACT 2600, Australia
[d] EIMF, School of GeoSciences, University of Edinburgh, Edinburgh, EH9 3FE, UK
[e] Department of Earth Sciences, Durham University, Science Labs, Durham, DH1 3LE, UK. E-mail: madeleine.humphreys@durham.ac.uk
[f] Centre for Ore Deposit and Earth Sciences (CODES), University of Tasmania, Hobart, TAS 7001, Australia
[g] Gallery of Natural Art, Richardson, TX 75083, USA

† Electronic supplementary information (ESI) available. CCDC 2422835. For ESI and crystallographic data in CIF or other electronic format see DOI: https://doi.org/10.1039/d5tb01061f

‡ Present address: School of Chemical Engineering, University of Queensland, Indooroopilly QLD 4068, Australia.

bioactivity leading to enhanced bone growth.[18] Synthetic silica-substituted apatite often contains carbonate due to its presence in the starting materials, but the carbonate contents and its structural position are rarely investigated and only mentioned in passing.[7,11,13,15,16,19–21] This characterisation gap stems from many challenges in measuring these aspects of carbonate incorporation in apatite.[22]

Carbonate could induce a first-order control on silica incorporation and stability, leading to more precise, reproducible, and biologically reliable silica-substituted apatites. Therefore, improved characterisation methods are desirable, particularly for the simultaneous incorporation of carbonate and silica into apatite, rather than for each anionic group individually.

In addition to the biological importance of apatite, this mineral occurs in natural terrestrial and extra-terrestrial rocks.[23] Apatite is the most common phosphate mineral on Earth, ubiquitous in igneous, sedimentary, and metamorphic rocks, and occurring anywhere from Earth's surface to the mantle. Natural igneous apatite contains many different minor elements, some of which offer potentially distinctive opportunities for charge-balancing carbonate and silica substitution. Carbonate-bearing apatite is common in carbonate-rich environments, particularly sedimentary (where it is informally known as francolite or collophane),[24] and in carbonate-rich igneous settings such as carbonatite systems and other alkaline rocks.[25] Carbonatite melts are rarely preserved in the geological record and any clues to their former presence (for example, detection of carbonate in apatite) may help unravel enigmatic geological history questions or identify potential mineralisation sources.[26] Furthermore, apatite can provide a record of mantle carbonate, with potential for understanding mantle metasomatism,[27] and the primary volatile contents of magmas such as kimberlites and carbonatites as well as other terrestrial magmas.[28] To facilitate that, we require a thermodynamically grounded understanding of substitution mechanisms for carbonate and silica in apatite.

Full characterisation of carbonate in apatite is challenging due to the typically small crystal size of synthetic apatite, and ubiquitous chemical and textural inhomogeneities in natural apatite. Most often, Raman and FTIR measurements on nano-scale material may include any by-products present; powder X-ray diffraction cannot determine the structural position of carbonate; and traditional SEM-EDS does not reliably reveal the presence of carbonate.[7,29,30]

Here we use a flux growth method to synthesise coarse-grained, homogenous, carbonate–silica-rich apatite at high pressure and temperature.[5,31,32] The large grain size permits characterisation using methods not usually available for finer-grained material, such as single crystal XRD (SCXRD),[5] wavelength dispersive spectrometry (WDS), attenuated total reflectance (ATR), and secondary ion mass spectrometry (SIMS). This thorough investigation allows us to elucidate a previously unconfirmed carbonate–silicate association in apatite, with potential implications for both synthetic bio-apatites and natural apatites. Minor and trace elements such as Mn, Mg, and Sr are commonly present in natural apatite,[33,34] and have been demonstrated to influence bioactivity in synthetic apatite.[14,21,35–37] As such, they were included here to demonstrate substitution feasibility during synthesis.

Methods and results

Synthesis

Crystallisation experiments were prepared and conducted at the Research School of Earth Sciences (RSES), the Australian National University (ANU). A powdered mixture of $CaCO_3$–54 wt%, $Ca_3(PO_4)_2$–27 wt%, $SrCl_2{\cdot}H_2O$–2 wt%, $MgCO_3$–6 wt%, $MnCl_2{\cdot}2H_2O$–3 wt%, SiO_2–2 wt%, NaCl–3.6 wt%, and KCl–2.4 wt% was prepared by immersion in acetone and mixing in agate mortar and pestle. After drying at 250 °C, 226 mg of the mixture were added into a 6.4 mm diameter swage-type nickel capsule,[38] together with 8 mg of graphite powder in order to control oxygen fugacity[39] at the C–CO_2 equilibrium, and generate additional CO_2 as a byproduct.[40] Several crystals of natural fluorapatite (unknown location in the Northern Territory, Australia, but likely from Mud Tank) were added to the mixture as seeds ($\leq$1 mm) to encourage new apatite crystal growth. The top of the capsule was pressed into a lip such that it would cold-weld under pressure and hermetically seal.

The capsule was loaded into a cylindrical 19 mm (3/4″) assembly consisting of an outer talc sleeve, graphite foil, and internal MgO components. The assembly was inserted into a pressure vessel and mounted inside an end-loaded piston cylinder apparatus with temperature and pressure controlled using automated in-house computer software (run number C5737–CAE72). Pressure was gradually increased to 500 MPa over 10 minutes, followed by an increase in temperature to 1100 °C over an additional 10 minutes. Upon reaching the desired conditions of 1100 °C and 500 MPa, the experiment ran for 144 hours, after which it was quenched by turning off the heating power and the water-cooled pressure vessel reached ~300 °C in roughly five seconds. Room temperature was reached in under a minute. Temperature was monitored using a type-B (Pt–Rh) thermocouple.

The quenched capsule interior contains three sections (Fig. 1a). The bottom third is dominated by newly-grown apatite crystals with their *c*-axes roughly aligned with the long axis of the capsule, and interstitial carbonate flux (Fig. 1b). Apatite is euhedral with well-developed crystal faces, typically 100 μm wide and up to 500 μm long. The middle section is dominated by dendritic quench crystals of calcite with fine-grained interstitial apatite (Fig. 1b). The top third contained a former vapour cavity which was filled with epoxy resin during mounting to mechanically stabilise the capsule contents (Fig. 1a).

Fourier transform infrared (FTIR)

Raw data, full quantification procedure, and calculations with intermediate steps for FTIR measurements are available as R code in the ESI,† and described below.

Attenuated total reflectance (ATR). FTIR measurements were obtained using a Bruker A590 infrared microscope connected to

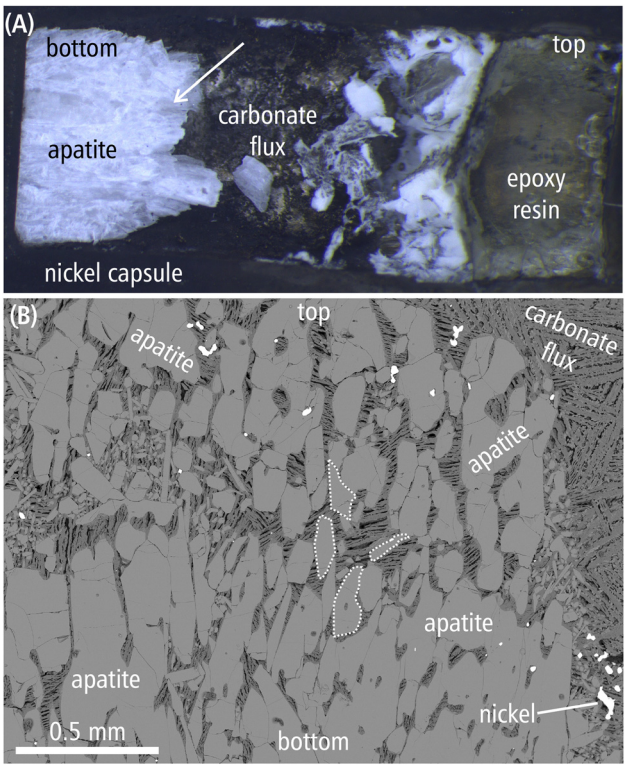

Fig. 1 (A) Reflected light image of the sectioned experimental capsule. Width is about 1 cm. (B) Backscattered electron image of a polished section showing apatite crystals with interstitial solidified carbonate flux exhibiting a dendritic quench texture, and some minor capsule-derived nickel fragments. Examples for four typical apatite crystals are outlined with a dotted line. Arrow in (A) shows approximate location of (B).

a N_2-cooled Bruker IFS28 spectrometer with a Hg–Cd–Te detector at RSES, ANU. First, we used attenuated total reflectance (ATR) mode using a Ge crystal objective on a polished surface of the apatite crystals. The analysed spot size was about 30 μm, much smaller than individual crystals, such that only apatite signal was obtained without contributions from the surrounding flux. Atmospheric, ATR, and baseline corrections were applied using the rubberband method in the OPUS software. Acquired spectra for the H_2O, carbonate, and phosphate regions are given in Fig. 2a, b, and c, respectively. H_2O and CO_2 contents were quantified using the Hammerli calibration.[41] For H_2O, Fig. 2a shows three different groups of analyses. Most of our sections are perpendicular to the *c*-axis, consistent with the general observation that the lowest amplitude H_2O peaks are associated with perpendicular section analyses.[41] Misoriented sections will show a spurious increase in H_2O peaks. Therefore, we only include the smallest peak group, for which H_2O (wt%) is calculated by $3.06 \times A_{H_2O}$, where A is the integrated area in the region between 3480 and 3600 cm^{-1}. Our range is shifted by 10 cm^{-1} from the Hammerli calibration[41] such that the entire H_2O peak is included, as often happens with variable apatite compositions.[42] Resulting value for H_2O contents is 0.34 wt% ± 0.03.

ATR measurement of CO_2 is much less sensitive to orientation than H_2O,[41] and although our measured sections are not perfectly perpendicular to the *c*-axis (as evident by the variance of H_2O peak intensity), we see no correlation between the spuriously high H_2O sections and CO_2 contents, suggesting that any systematic CO_2 errors caused by misorientations are smaller than the analytical noise. Therefore, we used the Hammerli equation for perpendicular sections: CO_2 (wt%) = $0.32 \times A_{CO_2}$,[41] resulting in CO_2 contents of 5.29 wt% ± 0.27, with the uncertainty being the standard deviation from 15 analyses. At 0.27/5.29 = 5.1%, this uncertainty is not as good as the <2% quoted in the original calibration[41] and could indicate minor carbonate content variability amongst the analysis spots in addition to orientation effects.

Transmission FTIR. Second, we used the polarised transmission mode on individual apatite crystals, which were separated from the experimental capsule and cleaned in acetic acid to remove the calcium carbonate flux. This acid treatment does not damage apatite crystals.[43] The crystals were mounted in epoxy for double polishing down to a thickness of several tens of micrometres. Even though polished, most crystals proved too thick and the FTIR signal saturated the detector. Only a single crystal was sufficiently thin such that the H_2O signal was not saturating the detector (Fig. 3a). Regrettably, we could not reach sufficient thinness such that CO_2 peaks remained unsaturated (Fig. 3b). Additionally, as this crystal was somewhat thinner, it had some leftover epoxy in the beam path which had to be corrected for by subtracting a pure epoxy signal. Measurement was conducted using a 100 × 100 μm aperture with 100 scans. The small crystal size and difficulty of manual positioning under an already unstable stream of dry air required the use of this larger aperture size, despite the recommended 50 × 50 μm size.[44]

Quantification of H_2O and CO_2 contents by transmission FTIR using the Wang[44] and Clark[45] calibrations requires knowledge of crystal thickness. The thicknesses of the doubly polished sections were obtained using a micrometer caliper, but the size and delicate nature of the crystals often led to failure, whereby apatite crystals shattered. However, as H_2O contents were known from the previous ATR measurement, we used the relationship H_2O (wt%) = $0.00119 \times A/d$ where A is the H_2O peak height at 3548 cm^{-1} (shifted by 8 cm^{-1} from the Wang calibration[44]) and d is sample thickness in cm.[44] Using H_2O (wt%) = 0.34 as obtained from ATR, the resulting thickness was 17.7 μm, which was slightly thinner than the thickness we expected the crystal to be, and in agreement with epoxy resin present in the beam path consisting a portion of total thickness. Using d = 17.7 μm, we used the Clark relationship CO_2 (ppm) = $0.0756 \times (A_{E\|c} + 2A_{E\perp c})/d$ where $A_{E\|c}$ and $A_{E\perp c}$ are the integrated areas between 1338 and 1567 cm^{-1}, respectively, and d is thickness in cm.[45] The resulting value is 3.13 wt%. Alternatively, using SIMS-obtained H_2O contents (0.21 wt%, see below) will lead to a lower carbonate estimate of ~1.9 wt%. However, as the top of the CO_2 peak between 1450 cm^{-1} and 1470 cm^{-1} is truncated due to detector saturation (Fig. 3b), this effectively leads to the unsatisfactorily constrained result that minimum CO_2 contents are anywhere between 1.93 wt% and 3.13 wt%.

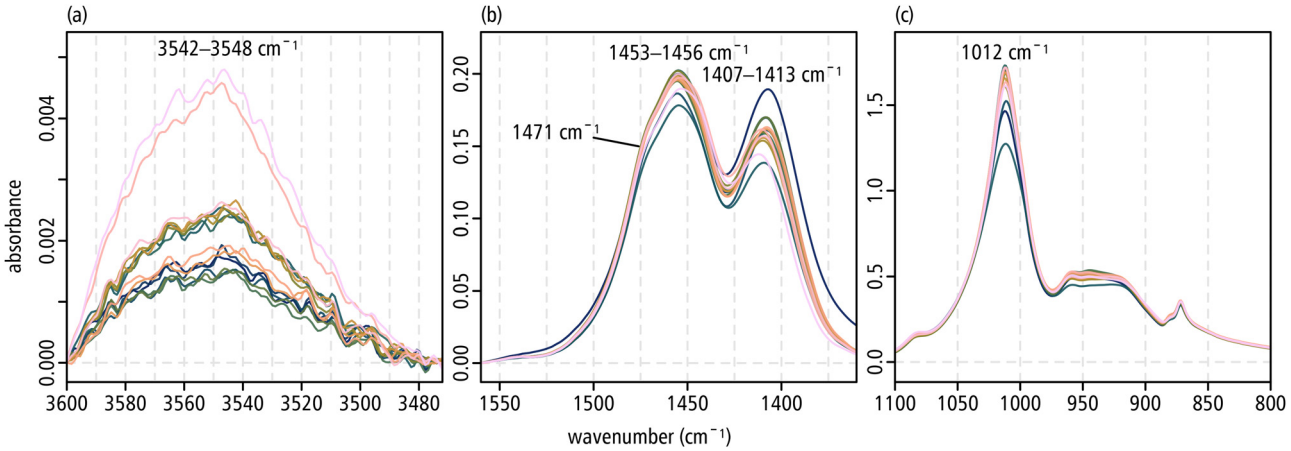

Fig. 2 Apatite FTIR-ATR spectra showing repeat analyses on different grains of the (a) OH^-/H_2O region, (b) ν_3 carbonate region, and (c) $\nu_1 + \nu_3$ phosphate region. For H_2O, only the low-absorbance group was used for quantification.

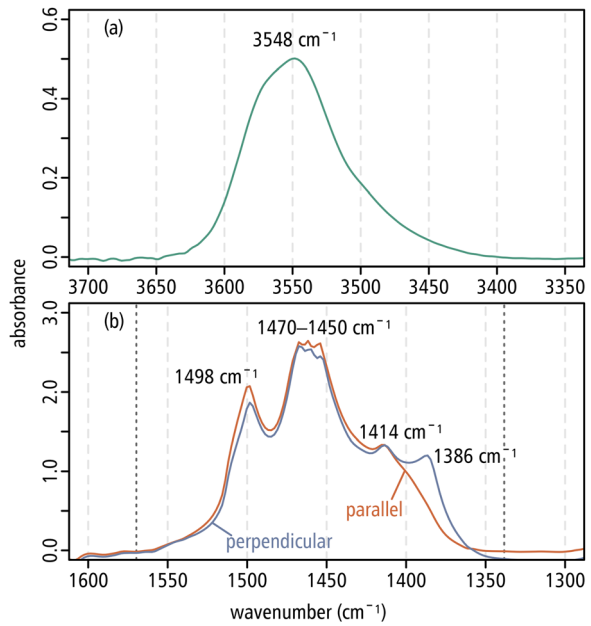

Fig. 3 Transmission FTIR spectra showing the (a) H_2O region, and (b) carbonate region in two different orientations. Jagged peak in (b) indicates detector saturation and truncation of peak height. Vertical dotted lines show boundaries for area determination.

Spectroscopic insights on the structural position of carbonate. Type-A and B carbonate substitutions are IR-active, most notably in the 1300–1600 cm^{-1} wavenumber region.[46] Previous attempts to assign each of the carbonate peaks to a specific substitution type have been inconsistent,[47,48] with peak positions and relative heights showing substantial variability as a function of whole-apatite composition (see review by Tacker[6] and multitudinous references therein). Nevertheless, the overall picture that emerges is that type-B substitutions are characterised by two strong peaks in the 1400–1450 cm^{-1} region whereas type-A substitutions span the entire range of 1300–1600 cm^{-1} wavenumbers.[5,46,49] Our FTIR measurements (ATR and transmission) are consistent with the presence of dominantly type-B as well as minor type-A substitutions (Fig. 2 and 3).

Electron probe microanalysis (EPMA)

Chemical analysis was conducted over three sessions at RSES, ANU, using wavelength-dispersive spectrometry (WDS) on a JEOL 8530F Plus electron probe microanalyser employing a Schottky field emission gun. For the first session, a section of the experimental sample was polished to 0.25 μm grade using diamond paste and then coated with a thin conductive carbon layer of ~15 nm. A full WDS spectrometer scan was conducted to identify elements for measurement (Fig. 4). Additional elements used in the synthesis experiment, capsule material, and common contaminants in natural apatite were included as well. Halogen diffusion is a known problem during microbeam analysis of apatite, mostly affecting F and Cl, and by the time-dependent variability of the matrix, all other elements.[50] In order to minimise systematic errors during apatite analysis, reference material for F was MgF_2 following previous recommendations,[51] and reference material for Cl was synthetic chlorapatite mounted such that an incident electron beam would be perpendicular to the *c*-axis.[52] To minimise halogen migration and the buildup of carbon contamination, special care was taken when navigating and selecting the measurement area. This was achieved by using the built-in optical microscope while blocking the electron path with the Faraday cup. A scanning electron image was primarily used at low magnification when necessary, while also reducing the probe current to below 1 nA. Fifteen points were selected on preferentially elongated grains to ensure that beam is mostly perpendicular to the *c*-axis. For each measured analysis spot, F, Cl, Ca, P, and Na were analysed first using a 10 nA beam defocused to 20 μm, followed by a second session for all other elements (except C) at 30 nA. Accelerating voltage was 15 kV. Full details of elemental analysis are given in the ESI.†

After the second session, the sample was repolished to remove the C-coat and the beam-damaged layer, cleaned with an Ar plasma glow discharge for two minutes, and coated with

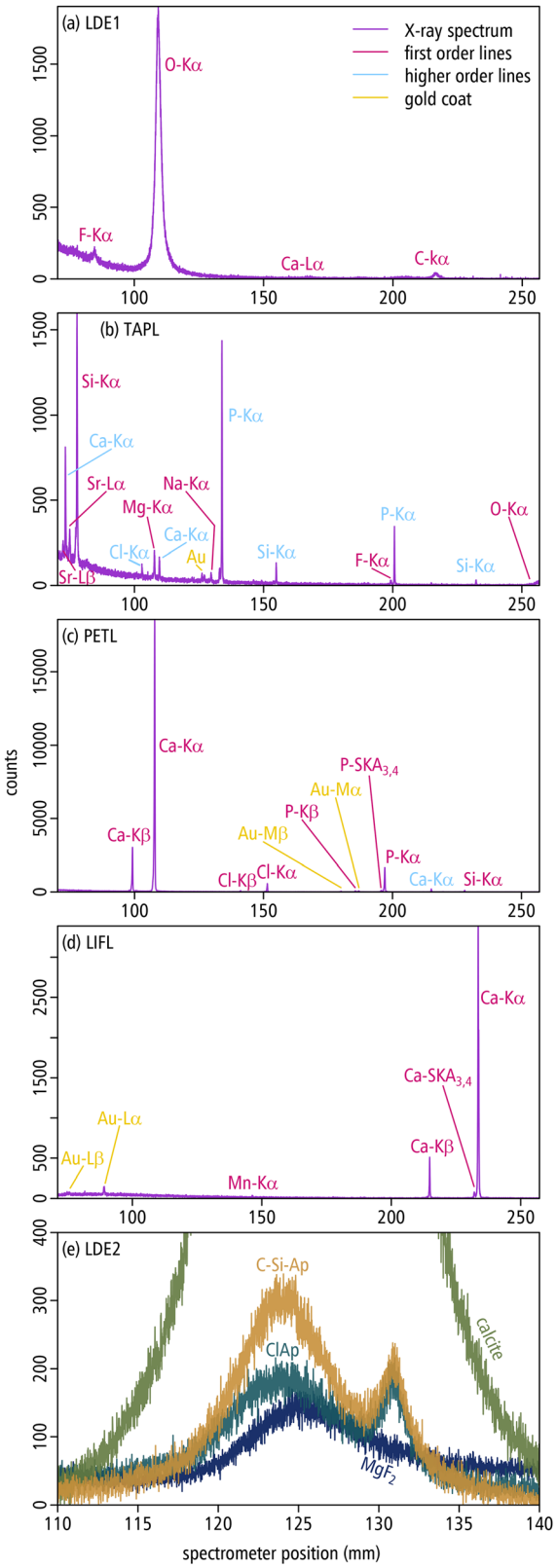

Fig. 4 WDS scans in order of increasing X-ray emission energy: (a) LDE1, (b), TAPL, (c) PETL, and (d) LIFL. (e) A WDS scan using LDE2 showing a closeup of the carbon peak in different materials. C–Si–Ap is the apatite synthesised herein, whereas the others are various reference materials.

3.5 nm thick gold using a Leica ACE600 sputter coater. A chlorapatite and an Iceland spar calcite reference materials underwent the same treatment. The sample and reference materials were loaded to the EPMA and left overnight in the sample chamber vacuum (better than 1.3×10^{-4} Pa) in an attempt to reduce analytical blanks that derive from carbon contamination. In the following day, the EPMA was set to 10 kV, and several WDS scans and test spot analyses revealed a persistent and consistent peak of the C X-ray K-α line of an uncertain provenance that appeared on all materials, regardless of their carbon contents (Fig. 4e). It is unknown whether this was a carbon deposit on sample surfaces, the spectrometer, some residual carbon inside the sample chamber, or a combination of both. Interestingly, the carbon peak position shifted between different materials for unknown reasons (*e.g.*, chlorapatite and MgF_2, Fig. 4e), indicating some relationship to the surface material. Therefore, chlorapatite was measured as a matrix-matched C blank in addition to the experimental unknown and the calcite reference material. Carbon dioxide blanks amounted to about 3.5 wt% CO_2 equivalent. A sequence of fifteen points on our synthetic apatite was bracketed by carbon blank measurements on C-free chlorapatite on both ends. Beam conditions for spot analyses were 20 nA beam current and 20 μm spot size.

Data from the three analytical sessions were averaged and then combined using CalcZAF 13.9.1.[53] Raw data from the first two sessions were corrected using an initial informed estimate of H_2O and CO_2 contents based on FTIR. Blank counts were subtracted from the unknown and calcite reference material measured in the third session to obtain CO_2 content. The resulting CO_2 content was iteratively used in the first matrix correction to improve accuracy of all other elements. CalcZAF was set to use the Bastin-PROZA φρZ correction (owing to its suitability for light elements[54]), and FFAST v2.1 mass absorption coefficients.[55] No spatial chemical gradients were detected during the analysis, demonstrating homogenous and unzoned crystals. Derived results are given in Table 1, with raw data and intermediate steps available in the ESI.†

Secondary ion mass spectrometry (SIMS)

Apatites were analysed for $^{1}H^{+}$, $^{12}C^{+}$, $^{16}O^{1}H^{+}$, $^{19}F^{+}$, $^{23}Na^{+}$, $^{25}Mg^{+}$, $^{30}Si^{+}$, $^{31}P^{+}$, $^{32}S^{+}$, $^{35}Cl^{+}$ and $^{44}Ca^{+}$ using a Cameca IMS 7f-Geo secondary ion mass spectrometer at the NERC Ion Microprobe Facility, University of Edinburgh, UK. The epoxy-mounted experimental run products were cleaned and coated with a thin layer of gold and stored overnight in an airlock under high vacuum prior to analysis. Analyses were performed in two modes. First, analyses were performed in positive ion high mass resolution mode (HMR, $M/\Delta M$ = 3000) and used a 5 nA, 13.5 kV ^{16}O primary ion beam generated with a Hyperion RF source and a spot size of around 10 × 15 μm. No energy filtering was applied. Higher mass resolution is advantageous in that S can be analysed simultaneously alongside other volatile elements as it resolves the large $^{16}O_2^{+}$ interference (ESI†). A 120 second pre-sputter with a 10 μm primary beam raster was used to clean the sample surface prior to each spot

Table 1 Chemical composition of synthesised apatite. Uncertainties given as 1sd. Atoms per formula unit (apfu) calculated on a single cation basis for a total of 5 apfu on the Ca-dominated M site

Chemical component	EPMA wt% (n = 15)	EPMA apfu	FTIR-ATR wt% (n = 15)	FTIR transmission wt% (n = 13)	SIMS wt% (n = 5)	SIMS apfu
CaO	53.805 ± 0.08	4.890				4.893
P_2O_5	35.058 ± 0.23	2.518			33.84 ± 0.35	2.432
SiO_2	2.434 ± 0.09	0.206			1.91 ± 0.09	0.163[d]
MgO	0.327 ± 0.01	0.041			0.31 ± 0.004	0.039[d]
MnO	0.176 ± 0.02	0.013				0.013
NiO	0.015 ± 0.02	0.001				0.001
SrO	0.482 ± 0.02	0.024				0.024
Na_2O	0.161 ± 0.03	0.026			0.08 ± 0.006[f]	0.026[f]
La_2O_3	0.036 ± 0.02	0.001				0.001
Ce_2O_3	0.061 ± 0.03	0.002				0.002
Nd_2O_3	0.044 ± 0.05	0.001				0.001
CO_2	5.049 ± 0.16	0.585	5.29 ± 0.27	>1.93 to >3.13	2.60 ± 0.08	0.302[e]
H_2O	0.338[b]	0.191	0.34 ± 0.03	0.21 ± 0.02 to 0.34 ± 0.03[b]	0.21 ± 0.02	0.118[e]
F	0.543 ± 0.07	0.146			0.57 ± 0.01	0.153
Cl	2.004 ± 0.04	0.288			2.35 ± 0.06	0.338
Total	99.853[a]				96.56[c]	

[a] Total percentage accounts for excess oxygen based on halogen contents. [b] Value and range based on transmission FTIR data. [c] Total percentage included other elements as analysed by EPMA, and SIMS values where present. [d] Derived from EPMA-based calibration. [e] Measured independently. [f] Measured using HMR, but of less confidence relative to LMR. Value used for stoichiometry is EPMA result. Also measured 0.01 wt% SO_3 using HMR, not shown in this table.

analysis. Analyte abundances were counted using an electron multiplier detector over ten cycles of the magnet, normalised to ^{44}Ca, and averaged. Total counting times per analysis ranged from 10 seconds for the ^{31}P to 30 seconds for the lowest count rate isotopes (^{12}C, ^{32}S, ^{35}Cl). Absolute concentrations were retrieved by linear calibration of $X/^{44}Ca \times CaO$, where X is the measured isotope, against a suite of seven large, well-characterised, gem-quality apatites,[28,56] except for ^{35}Cl which shows a polynomial calibration curve (see ESI†). The apatite reference materials were previously characterised by other methods including LECO (for C, S), thermal conversion elemental analyser (TC/EA, for H_2O), EPMA (for halogens, major and minor elements), laser ablation inductively coupled plasma mass spectrometry (LA-ICP-MS; for trace elements), SIMS (to check for volatile homogeneity), and FTIR-ATR (for volatiles).[28] The calibration apatites have water contents ranging from <0.01 to 1.40 wt% H_2O and carbon contents up to 0.81 wt% CO_2 (see ESI†).

Backgrounds for all elements were assumed to be zero, except for OH, as H_2O in the vacuum results in a non-negligible signal. The calibration standards were mounted in indium, which gives comparably low OH backgrounds of *ca.* 0.03 wt% H_2O equivalent. The OH signal of end-member chlorapatite, which was mounted in resin and assumed to be anhydrous, was used to correct for OH backgrounds in all the epoxy grain mounts (ESI†). However, for these mounts the OH background was excessively high, amounting to at least 0.56 wt% H_2O. This H_2O background decreased during the time the sample spent in the sample chamber, which has a higher vacuum (roughly 2×10^{-8} mbar) than the air lock where samples are stored (3×10^{-7} mbar). For example, seven repeat analyses of our synthetic apatite resulted in apparent water contents (before background correction) decreasing from 1.14 to 1.02 wt% over the course of an hour.

For that reason, we measured H_2O contents again in a different mode using ^1H in addition to $^{16}O^1H$, and applied energy filtering to reduce the vacuum contribution to the H and OH background. Energy filtering selects ions with higher energies (75 ± 25 eV) and is therefore less susceptible to changes in ionisation potential, or presence of interfering dimer ions, and thus more resistant to matrix effects.[57] To compensate for signal loss due to energy filtering, analyses were performed in low mass resolution (LMR) mode. All other elements, except Na, which was present at very low levels, and S, which suffered from a large $^{16}O_2^+$ interference, were also re-measured. Results were generally very similar (as expected, considering that we used the same calibration standards) except for Cl and CO_2, which were on average 9% and 14% lower, respectively, and P, which was 8% higher. This suggests the presence of some unresolved matrix effects, as the composition of our apatite is very different to any of the calibration standards. Overall, we view the results from LMR as more reliable given the tendency for greater matrix effects under HMR mode (Table 1).

As to water, the ^1H and $^{16}O^1H$ backgrounds for the indium-mounted standards were 0.011 and 0.037 wt% at most, respectively, based on the values of the standard with lowest H_2O signal (PAN2). The $^{16}O^1H$ background on anhydrous, resin-mounted chlorapatite was equivalent to 0.29 wt% (compared to 0.031 wt% for ^1H) but using this value as the background for our resin-mounted synthetic apatite resulted in H_2O values considerably higher than using ^1H (mean 0.32 wt% *vs.* 0.21 wt%). We therefore used a background value that results in $^{16}O^1H$ measurements matching those by ^1H (ESI†), but essentially, we adopted the ^1H values as being the most accurate. Another outcome of the comparison between ^1H and $^{16}O^1H$ measurements is that the calibration for ^1H appears to be slightly non-linear and is better using a polynomial calibration (see ESI†). However, the effect on

Table 2 Selected bond lengths and bond-valence analysis for cations and anions in carbonate-bearing apatite from SCXRD; 2.7 Å cut-off for Ca–O bonds

Bond	Length (Å)	Valence	Bond	Length (Å)	Valence
Ca1–O1 (×3)	2.4054(17)	0.3	Ca2–O2	2.316(3)	0.37
Ca1–O2 (×3)	2.457(3)	0.26	Ca2–O3 (×2)	2.3399(16)	0.35
⟨**Ca1–O**⟩	**2.431**	∑ = **1.67**	Ca2–Cl1 (×2)	2.5019(19)	0.22
Ca1–O4 (×3)	2.51(4)	0.26	Ca2–O3 (×2)	2.5384(16)	0.21
Ca1–O5 (×3)	2.56(3)	0.2	⟨**Ca2–φ**⟩	**2.439**	∑ = **1.94**
			Ca2–O4	2.50(6)	
P–O3 (×2)	1.5276(16)	1.27	C1–O5	1.304(10)	1.26
P–O1	1.540(2)	1.23	C1–O4	1.305(10)	1.26
P–O2	1.541(2)	1.23	C1–O3	1.306(10)	1.26
⟨**P1–O**⟩	**1.534**	∑ = **5.01**	⟨**C1–O**⟩	1.305	∑ = **3.78**

apatite with H_2O contents <0.5 wt%, such as the one from this study, is minimal.

Single crystal X-ray diffraction (SCXRD)

Individual apatite crystals were separated from the capsule and mounted on MiTeGen micromount loops. The mounts were transferred onto the goniometer of an Agilent Supernova dual-source diffractometer for single crystal X-ray diffraction data collection. The diffractometer was cooled by an Oxford Cryosystems open flow N_2 cooling device.[58] A hemisphere of data was collected at 150 K using mirror monochromated Mo K-α (λ = 0.71073 Å) radiation out to very high resolution of 0.55 Å. Data collected were processed using the CrysAlisPro package[59] (version 1.171.35.8), locating 7511 reflections with an R_{int} of 0.0230. Subsequent structure solution refinement proceeded *via* a dual space algorithm using SHELXT[60] followed by structure refinement in SHELXL[61] in the SHELXLE[62] environment. All atom positions were refined with anisotropic displacement parameters except for the C atom (C1) in the T′ site and its associated O atoms (O4 and O5).

The refinement converged to final R_1 and wR_2 values (all data) of 0.0226 and 0.0504, respectively. Further details of data collection and structure refinement are provided in the ESI.† Atomic coordinates and displacement parameters are shown in the ESI,† and selected bond lengths and a bond valence analysis are given in Table 2 using parameters of Gagné and Hawthorne[63] for all bonds except Ca–Cl, for which Brese and O'Keeffe parameters were used.[64] The CIF of carbonate–silicate-bearing apatite is deposited in the Cambridge Crystallographic Data Centre (CCDC) with sample submission code 2422835.

Crystal structure and locating carbonate groups. The crystal structure of carbonate-bearing apatite has a similar structural framework to previously defined crystal structures of apatite, crystallising in hexagonal space group $P6_3/m$ with two M sites, one T site, three framework O sites, and one X site as previously described.[5,31] However, the refinement of C and O positions pertaining to a type-B CO_3^{2-} trigonal group, located in vacancies on what would be alternating sides of the TO_4 tetrahedron, is previously undescribed (Fig. 5a). The C site is designated as the T′ site. The TO_4 and T′O_3 groups cannot be present in the same position at the same time due to space constraints and the sharing of one of the two O3 site positions. Allowing the P-dominant TO_4 site to refine its electron occupancy yields a 90.1(5)% occupancy by P, which when vacant is occupied by alternating $^{B}CO_3^{2-}$ triangles. A free variable refinement is only possible when there is a single atom in the site, so the occupancy of the site was subsequently fixed as 80% P and 10% Si, with the remaining 10% occupancy of T + T′ provided by C. The C site and associated O4 and O5 atoms were refined with a fixed low occupancy of 5% based on the refined 90.1(5)% T site occupancy, which totals the remaining 10% T + T′ occupancy as the C position alternates sides of the vacant TO_4 site (Fig. 5a). C–O bond lengths for all three O atoms were refined using a soft constraint of 1.30(1) Å due to otherwise unacceptably high displacement parameters. The two additional sites are required as the C–O bond length of 1.305(10) Å is ∼0.23 Å shorter than the average P–O bond length of 1.534(9) Å. However, the $O3_{bonded}$ site is positioned in such a way that no second site is required when the CO_3^{2-} group is present; the C–$O3_{bonded}$ length is 1.306(10) Å. The O1 site of the TO_4 tetrahedron is equivalent to the O5 site of the $^{B}CO_3^{2-}$ group, and the O2 site to the O4 site, respectively. This solves a previously encountered challenge where a type-B carbonate was suggested, but its O1 and O2 sites could not be adequately resolved.[5] Only one of the two O3 sites that supports the TO_4 group is required for the $^{B}CO_3^{2-}$ group, and each takes turns at being the site that is occupied when C is present (Fig. 5a). The other O3 site now does not have an anchoring high-charge cation nearby and is vacant in the scenario (10% of the time) when the opposing CO_3^{2-} is present (distance to the non-bonding O3, C–$O3_{absent}$ length, is 1.87(8) Å), as previously hypothesised.[65] If this O3 were present, its bond-valence would be very low (0.56 valence units, formed by two bonds to Ca2). In this scenario, the presence of the $^{B}CO_3^{2-}$ group prevents bonding of an additional H to the O3 site due to lack of space. Despite this, because this vacancy occurs infrequently, there is no noticeable electron density loss for O3 in the refined crystal structure.

Determination of the X (channel) site occupancy is more difficult. A single site was initially refined as a Cl^- anion in the crystal structure with an occupancy of 0.321(4), corresponding to $Cl_{0.64}$ per formula unit. Attempts to refine the site as a mixed occupancy site with Cl and either F or O (as OH^-) were unsuccessful due to the relatively low electron density in the site. However, this amount of Cl was too high compared to values we obtained by other analytical methods (see below), so a fixed refinement of Cl, F, and OH was undertaken in a 4 : 3 : 3 ratio of the Cl : F : O(H) atoms. This led to slightly higher (0.1%) *R* indices than allowing for a free refinement of Cl solely, but is a better representation of the crystal chemistry as derived from microanalytical data.

As shown above, FTIR analyses suggest that a type-A carbonate anion could also be found partially occupying the channel site. Although no such carbonate group was clearly demonstrated, O3 atoms are typically closest to the X site anions, with distances greater than 3.05 Å. An O3 vacancy could then in turn generate free space in which a monoatomic anion such as Cl^- or F^- could be replaced by an entire $^{A}CO_3^{2-}$ group (Fig. 5b). Typically, type-A carbonate is oriented vertically with respect to

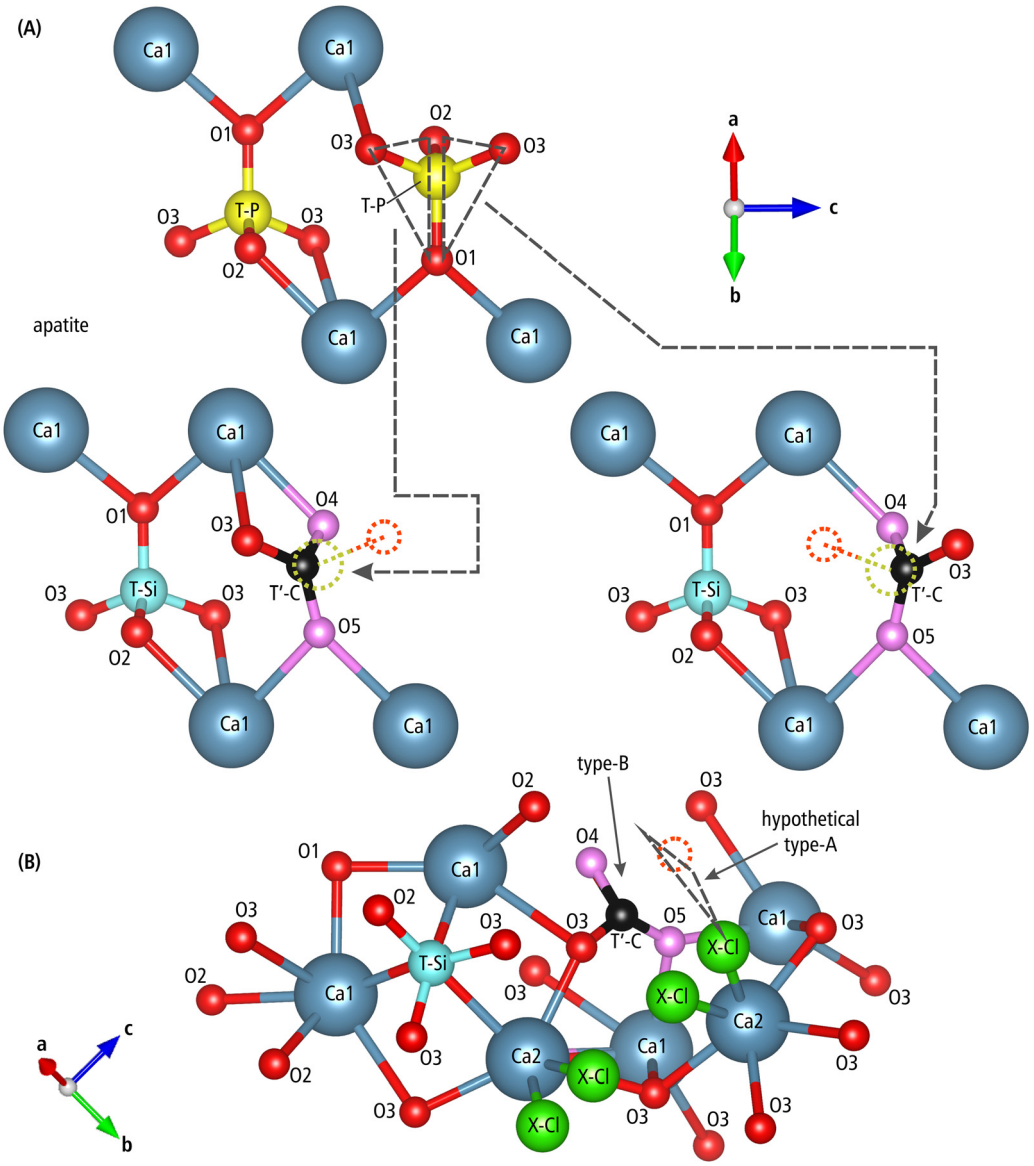

Fig. 5 Crystal structure of our apatite interpreted using a combination of compositional and structural data obtained in this study. (A) Replacement of a phosphate site (top) with two possible orientations of carbonate (bottom), each occupying a face of the former phosphate tetrahedron, marked by the grey dashed triangles and lines. The newly formed O3 vacancy is marked by the dashed red circle, and the former P position in the T site is marked by the dashed mustard yellow circle. Note that the charge-balancing silicon atom does not have to be adjacent to carbonate, but here they are shown together for illustration purposes. (B) Structural relationship between the newly-formed O3 site vacancy (dashed red circle) and the halogen channel defined by alignment of X-Cl anions (green)—demonstrated here with a simplified chlorapatite model—showing possible free space in which a type-A carbonate group might fit, with the triangle plane mostly perpendicular to the *c*-axis.

the *c*-axis, with several rotations along the horizontal axis identified (*e.g.*, A1 and A2).[31,66] Other studies have suggested other orientations for $^{A}CO_3^{2-}$, for instance as triangles perpendicular to the *c*-axis,[67,68] which is not conclusively observed in the crystal structure we determined for our synthesised apatite. Nevertheless, stoichiometric constraints may require the presence of type-A carbonate, with this horizontal orientation being the most probable (see below). If such an orientation is proven to exist (see our proposal in Fig. 5b), we suggest that type-A3 would be an appropriate name for it. The highest electron density peaks and troughs remaining in the Fourier map have a magnitude of just $\sim$0.5 e^- and there is little scope for determining the positions of O atoms arranged in a triangle around a postulated central channel atom. It is worth noting that the anisotropic displacement parameters of the X site reveal an oblate or tabular shape, suggesting that there is variability of the position location (*i.e.*, the electron density is not focused to a spherical point), or the site is disordered off the channel axis, which could be related to the presence of minor $^{A}CO_3^{2-}$. Two electron density peaks of 0.40 and 0.29 e^- are found $\sim$1 Å from the X site, which could be related to the possible H site when the OH group is substituting or possibly to O anion sites if C were to substitute, but there is limited crystallographic evidence for either.

In this work, we propose a new type-B4 substitution for CO_3^{2-}, with a coupled replacement of two phosphate groups with one silicate and one carbonate group. Previous researchers have focused primarily on M site substitutions rather than further T site substitutions for type-B carbonate, where carbonate is located roughly at the location of the phosphate groups. For example, it was proposed that B1, B2, and B3 substitutions all involve creating Ca^{2+} vacancies for charge balance.[69] Other unnumbered type-B substitutions were identified, often with vacancy formation on the X site, or substitution of Ca with Na.[32,42,70] Of these three, the B3 substitution is closest to what we observe in our study: Su *et al.* described $^{B}CO_3^{2-}$ on a triangular face of the phosphate group, without crystallographic evidence.[69] Our work shows that charge can be balanced by having a more negatively charged anionic group (in this case orthosilicate) replacing phosphate in a 1:1 ratio with the amount of replaced carbonate.

Discussion

Analytical challenges

Chemical compositions of our synthetic apatite measured using the different methods described here do not agree. Carbonate by SIMS and transmission FTIR at (2.6 wt% and >1.9–3.3 wt%, respectively) is around half the measured contents by EPMA and FTIR-ATR (≥5 wt%). Elucidating the discrepancy is difficult. Carbonate analysis by SIMS routinely delivers good calibration curves. The calibration materials have been analysed in bulk by LECO mass analyser for total C, and by SIMS to check for homogeneity. Similarly, the reference material H_2O contents were measured by TC/EA and have likewise been checked for homogeneity. Despite this, the CO_2 content by SIMS is higher than the analysis was calibrated for, which raises the question of whether matrix effects could affect analysis of more C-rich apatites, particularly in HMR mode (see earlier discussion). We note that this lower CO_2 content is not sufficient to complete analytical totals to 100%, if substituted into the EPMA analysis, instead leading only to about 98.3%. This value is not adjusted for excess oxygen–halogen correction, and real analytical totals would be slightly lower.

The source of the C K-α peak on EPMA remains a mystery (*e.g.*, the carbon peak observed for the undoubtedly C-free MgF_2 in Fig. 4e). It does not result from carbon build-up at the analytical spot, as the appearance of a contamination ring around the spot after many minutes of electron beam irradiation only coincides with a very modest increase in C counts.[71] The measured signal is present from the start, and only acquired for 30 seconds such that any carbon build-up is negligible. We assumed that it does not depend on the material measured, and used it as a blank (but note difference in carbon peak position in Fig. 4e). The validity of this assumption is untested, and although blank corrections are occasionally used,[72] to the best of our knowledge there has been no study to independently validate the method. The choice and characterisation of a blank is important: we used a synthetic fluorapatite together with the above-described chlorapatite, but it had slightly higher C counts. A subsequent examination by ATR revealed it to contain a small amount of solid solution carbonate (not shown here, but the FTIR signal was similar to Fig. 2b). This was surprising given that the fluorapatite was crystallised from a molten flux in an open crucible at 1650 °C. This serves as a salient reminder never to assume that apatite is carbonate free, particularly when said apatite is to be used as a reference material (see retained carbonate during LECO analysis leading to spuriously low CO_2 contents[46]). Moreover, C K-α peak positions and width may shift depending on the measured material,[73] and using peak height alone for quantification may not be ideal. Another source of error could arise from the use of calcite as a carbon reference material. Carbon counts on calcite are known to decrease during beam exposure, which could lead to an overestimation of carbonate contents in test samples.[74] However, our analytical conditions (20 nA beam current and 20 μm spot size) result in the same beam density as the recommended values (5 nA and 10 μm[74]), hence incorrect measurement of carbon on the reference materials is unlikely to be a major issue. Alternatively, CO_2 contents in calcite are about an order of magnitude higher than those measured in our apatite, and taken together with uncertainty on blank correction (at a very substantial ~3.5/5.0 = 30% of our measured value) could also lead to erroneous measurements.

Fourier transform IR analysis also had its own challenges. Transmission FTIR for our carbonate-rich apatite always saturated the detector, even to exceptional thinness of ~18 μm in which it became nearly impossible to manually handle the crystals. In contrast, ATR measurement did not saturate the detector and only required a readily-achievable polished section, but it has its own challenges of unconstrained crystal orientation. We also note that our peak positions for phosphate, carbonate, and OH^- do not match those given in the calibrations, and our measured CO_2 content was close to 5 wt%, significantly exceeding the calibration range of the original reference materials (up to ~1.1 wt%).[41] Given that peak positions and spectrum shape might shift and change depending on the orientation of polarising molecular species (such as carbonate),[5,6] one cannot expect a perfect correlation between the calibration standard and the test sample, unless the matrix is identical. This problem is exacerbated by minor element content in apatite, particularly Sr and Mn which are known to cause peak shift.[42] Finally, unlike SIMS and EPMA analysis, no primary or secondary reference materials were measured during FTIR analysis.

Here, XRD revealed a new type of structural position for carbonate in a site labelled as the T′ site. Likewise, OH^- probably has a unique structural position and orientation due to the presence of fluoride, chloride, and potentially type-A carbonate, although no conclusive crystallographic evidence was observed for any type-A carbonate in the X site. Nevertheless, differences are likely to be minor, as ATR H_2O contents are subsequently used in EPMA calibration, and ATR CO_2 contents are very close to those measured by EPMA, which itself leads to 99.85% totals, a remarkable result for an EPMA measurement of apatite. We note that the possible variable structural positions of

Table 3 Chemical composition electron density comparison of single-crystal X-ray crystallography with other techniques. M1 and M2 sites calculated as electrons per cation, T, T′ and X as electrons per atom

Site	Element in SXRD model	Elements contained (EPMA)	$e^-_{X\text{-ray}}$	e^-_{EPMA}	$e^-_{FTIR\text{-}ATR}$	$e^-_{FTIR\text{-}Trans}$	e^-_{SIMS}
M1 + M2	Ca	Ca, Mg, Mn, Ni, Sr, Na, La, Ce, Nd	90	90.118			
T	P, Si	P, Si	40.2	40.657			38.733
T′	C	C	1.8	3.509	3.677	2.266	1.806
T + T′	T: P, Si T′:C	P, Si, C	42	44.166			40.539
X	Cl, F, OH	Cl, F, OH, □	11.9	7.739			8.056

carbonate and OH^- are not relevant for SIMS analysis. Additionally, this leads to apatite with a negligible charge imbalance. H_2O as measured by SIMS is very similar to FTIR measurement. Overall, our structural model fits the measured XRD data very well, particularly for carbonate on the T site (type-B). Derived electron densities mostly agree with values expected from chemical data as measured by the other methods (Table 3), with the caveat that the presence of X site carbonate (type-A) remains uncertain.

Apatite stoichiometry and charge balance

There are several ways to calculate a stoichiometric mineral formula for apatite,[75] but they are inadequate for our purposes: they do not account for carbonate (often not quantitatively measured in apatite), assume that the total ions in the X site must sum to 1 atoms per formula unit (apfu), and only consider F^-, Cl^-, and OH^- in the X site (with H_2O, again, typically not quantitively measured). However, in our study both CO_2 and H_2O are quantitatively measured, permitting us to derive a more constrained mineral formula. Stoichiometric calculations are guided by quantitative measurements, and as thoroughly discussed above, all methods have their advantages and disadvantages.

Calculation using EPMA and FTIR-ATR data. Some assumptions must be made about site occupancy. The M site can contain vacancies, but in our case it is unlikely to occur as our system is highly calcic, with $CaCO_3$ being the dominant flux component such that the thermodynamic activity of the CaO component is nearly as high as possible. Furthermore, the electron density on the M site as measured by SCXRD is modelled as pure Ca, and is consistent with full occupancy at 5 apfu, consisting of primarily Ca with minor contributions from lighter (Na, Mg) and heavier cations (Sr, Mn). Consequently, we begin by normalising all M site cations to 5. For the next step, the T site is filled with P, Si, and C in order to complete it to 3 apfu, and the X site is filled with F, Cl, OH, and—using EPMA data—any leftover C. Oxygens are assigned following the measured Si, P, and C contents as the orthophosphate, orthosilicate, and carbonate groups (PO_4^{3-}, SiO_4^{4-}, and CO_3^{2-}, respectively). The resulting stoichiometry is M: $(Ca^{2+}_{4.890}Mg^{2+}_{0.041}Mn^{2+}_{0.013}Ni^{2+}_{0.001}Sr^{2+}_{0.024}Na^{+}_{0.026}La^{3+}_{0.001}Ce^{3+}_{0.002}Nd^{3+}_{0.001})_{\sum 5}$, T: $(P^{5+}_{2.518}Si^{4+}_{0.206}C^{4+}_{0.276})_{\sum 3}O^{2-}_{11.724}$, X: $([CO_3]^{2-}_{0.309}Cl^{-}_{0.288}OH^{-}_{0.191}F^{-}_{0.146})_{\sum 0.934}$. This site assignment results in 25.923 positive charges and 25.928 negative charges, with only 0.02% mismatch between the two. This result demonstrates the primary charge-balanced substitution occurring on the T site: $2PO_4^{3-} \rightarrow SiO_4^{4-} + {}^{B}CO_3^{2-}$. However, the EPMA/ATR-derived value of ~5 wt% only accounts for 0.206 apfu of carbonate on the T site. An additional charge-balanced substitution introduces carbonate to both T and X sites:[5,70] $PO_4^{3-} + X^- \rightarrow {}^{A}CO_3^{2-} + {}^{B}CO_3^{2-}$, with more carbonate in the X site (0.309 apfu) than in the T site (0.276), consistent with recent determinations on synthetic carbonate-bearing apatites.[48] Alternatively, there could be an atom-by-atom replacement of Si by C without oxygen vacancy formation—explaining C > Si on the T site—as was recently demonstrated for britholite, an apatite-group silicate.[68] These are theoretical exchange vectors, and in a complex material like the apatite synthesised here, they could both be equally applicable.

Although the silica–carbonate substitution has been suggested before, it lacked rigorous confirmation.[15,17,65,76–80] Our combined crystallographic and chemical results confirm it. Previous work[32,81] suggested that carbonate is accommodated *via* the exchange ${}^{A}CO_3^{2-} \rightarrow 2OH^-$, where a vertical carbonate group takes the space of two hydroxyls. However, we find that occupancy on our channel site is close to one. If this proposed exchange is correct, then the X site needs to be deficient by at least half its carbonate contents (*i.e.*, 1–0.309/2 = 0.8455). Evidently, this is not the case, raising the possibility of a horizontally oriented trigonal carbonate group, potentially enabled by the newly-formed type-B oxygen vacancies (Fig. 5b and above discussion on O3 vacancies), as opposed to a predominantly vertical orientation.[32,67]

Calculation using SIMS. We performed an additional stoichiometric calculation using SIMS data, with EPMA data to fill in missing minor elements which were not analysed using SIMS. When normalising all large M site cations to 5, P + Si on the T site equal 2.594 apfu. Carbon contents are now lower compared to EPMA data at 0.301 apfu, which only fill the T site to 2.896 apfu and cannot complete it to the theoretical 3 apfu. It is unknown whether this results from too low Si + P, or too low C. The X site is likewise unfilled, with OH, F, and Cl only accounting to 0.609 apfu, suggesting the presence of substantial vacancy fraction.[28] The full stoichiometric formula is M: $(Ca^{2+}_{4.893}Mg^{2+}_{0.039}Mn^{2+}_{0.013}Ni^{2+}_{0.001}Sr^{2+}_{0.024}Na^{+}_{0.026}La^{3+}_{0.001}Ce^{3+}_{0.002}Nd^{3+}_{0.001})_{\sum 5}$, T: $(P^{5+}_{2.432}Si^{4+}_{0.163}C^{4+}_{0.302})_{\sum 2.896}O^{2-}_{11.594}$, X: $(Cl^{-}_{0.338}OH^{-}_{0.118}F^{-}_{0.153})_{\sum 0.609}$. This site assignment results in 24.111 positive charges and 23.172 negative charges, with a substantial 4.05% mismatch between them.

The reasons for the poor stoichiometry derived from SIMS data are not entirely clear. The combination of inferred vacancies in both T and X sites, the low analytical totals, and the large mismatch between positive and negative charges indicates that carbonate contents are probably underestimated. The likely cause is carbonate being outside its calibrated range, with the possibility of a non-linear calibration that is not resolvable

using the range of standards available. The richest CO_2-bearing apatite used in the SIMS calibration curve had 0.81 wt% CO_2, roughly 3 times lower than our CO_2 contents as measured by SIMS, and more than 6 times lower than CO_2 as measured by EPMA and FTIR. Nonetheless, the type-B carbonate inferred from SCXRD is much closer to the low SIMS-derived CO_2 contents, suggesting a different matrix effect during SIMS analysis for type-A *versus* type-B carbonate.

Which analytical method is better?

It is difficult to point out one analytical method that is ideal. SIMS is well calibrated with primary secondary materials measured during analysis. However, it still relies on Ca from EPMA analysis as an anchor point for other elements such as Si and P. It also results in a stoichiometric composition that is not as good as other methods. On the other hand, EPMA suffers from substantial blanks, only a two-point calibration using CO_2-rich calcite, and potential issues with occasionally arbitrary matrix correction procedures.[68] Measurement using FTIR is similarly problematic with transmission techniques leading to clipped peak heights and ATR relying on absolute contents with no concurrently-measured reference materials. Peak positions change, leading to further uncertainty. Nevertheless, stoichiometry based on EPMA and FTIR is, in our case, better than that derived from SIMS.

The inconsistent CO_2 contents presented here do not affect our conclusion regarding the charge balanced substitution ($2PO_4^{3-} \rightarrow SiO_4^{4-} + CO_3^{2-}$), because only 1.78 wt% CO_2 is required to charge balance the measured 2.435 wt% SiO_2, and even the low CO_2 contents measured by SIMS are more than sufficient.

Based on our results, and acknowledging that CO_2 is rarely measured in apatite, we suggest that a Si-bearing T site that does not sum to 3 apfu should be suspected to contain carbonate.[65,82] We recommend that in these cases, further investigation to confirm and quantify the presence of carbonate be conducted.

Implications for biological applications

Our confirmation of the silica–carbonate substitution in apatite opens an avenue for targeted synthesis methods.[37,49,83] Although silica substitution is acknowledged as beneficial for reaction rates, the actual charge-balancing and its implications for bioactivity are rarely discussed. Most commonly, silica is claimed to be substituted by either:[8,11,12,20,29,30,78,84,85]

$$P^{5+} + OH^- \rightarrow Si^{4+} + X_{vacancy}, \quad (1)$$

$$Ca^{2+} + P^{5+} \rightarrow Ln^{3+} + Si^{4+}, \quad (2)$$

where Ln indicates a lanthanide or yttrium,[86]

$$2P^{5+} \rightarrow Si^{4+} + S^{6+}, \quad (3)$$

or by our proposed[65]

$$2P^{5+} + O^{2-} \rightarrow Si^{4+} + C^{4+} + O_{vacancy}. \quad (4)$$

Both carbonate and orthosilicate enter the T site, which led some authors to suggest that the two anionic groups compete.[11,13,36,79] Our results show that there is no competition—divalent carbonate and tetravalent orthosilicate balance the charge such that their average is the same as the trivalent phosphate, and their combined presence may enhance substitution of both.

Biocompatibility is enhanced by crystal structure defects caused by silica substitution.[10,12] As each silica substitution pathway would result in different structural defects, it would be naïve to assume that their bioactivity is similar. Carbonate behaviour is dissimilar, as it can be charge balanced by a variety of substitutions (such as $Ca^{2+} + PO_4^{3-} \rightarrow Na^+ + CO_3^{2-}$).[21,70,76] We call upon other researchers to tweak their starting compositions to achieve a particular apatite composition, thoroughly measure the composition, and investigate which substitution is most beneficial for medical applications. An instructive example of that of Gibson *et al.*[8] which synthesised high temperature silica apatite at 1200 °C. They were unable to detect any carbon using a C–H–N analyser, and inferred that their silica was incorporated using the X site vacancy path (1). However, their FTIR spectra clearly indicate the presence of carbonate, leading to the possibility that silica substitution was controlled by carbonate *via* path (4), but was overlooked. This demonstrates the thermal stability of this substitution,[16,76,87] potentially by migration of carbonate from the T site to the X site (*i.e.*, transformation of type-B to type-A[88]), and the challenge of its detection by combustion methods such as C–H–N measurements. On the other hand, other syntheses with both carbonate and silicate at high temperature led to complete removal of carbonate, whereas silica was retained.[77,89] This was occasionally explained by the formation of silicocarnotite from the excess silica, now that the apatite has been decarbonated and silica is no longer charge-balanced.[12,76–78,84,90] The reasons for this discrepancy are unclear and require further study. Elsewhere, FTIR spectra obtained from silica-substituted apatite by Moreno-Perez *et al.* contains a clear carbonate signal, but this finding is omitted and not discussed in their study.[30]

Carbonate and silica in natural apatite

That apatite contains detectable carbonate, which is not necessarily charged balanced by silica, is well established.[6] However, natural systems are inherently silica-rich. The substitution reaction written in pure oxide thermodynamic component terms is:

$$Ca_5(PO_4)_3X + SiO_2 + CO_2 \rightarrow Ca_5(PO_4)(SiO_4)(CO_3)X + P_2O_5$$

Assuming that P_2O_5 activity is nearly constant at any apatite-saturated conditions, the dominant controls on this substitution are SiO_2 and CO_2 activities. Many magmatic systems are SiO_2 saturated or nearly so, and CO_2 solubility is sufficiently low to saturate as well. However, the total amount of CO_2 in these systems is usually minor such that any substantial silica–carbonate substitution is small. Nonetheless, we expect that most igneous apatites in silica saturated systems, if thoroughly investigated, will reveal some amount of charge-coupled silica and carbonate. The presence of this type-B carbonate may (1) indicate some presence of type-A carbonate,[91] and (2) introduce systematic errors to stoichiometry determinations because

C-associated oxygen is not considered during oxygen normalisation. If type-A carbonate is present to any significant amounts, this may undermine efforts to use thermodynamic models of F^-, Cl^-, and OH^- X site occupancy to infer apatite formation conditions such as temperature, pressure, and system composition.[33,42,51,92]

Our experimental results show that silica substituted carbonate apatites are in equilibrium with a liquid which is not significantly different from natural carbonatite melts, at geologically reasonable conditions. A lamentable property of carbonatite melts is that they are rarely, if ever, preserved in the geological record.[93] It is only when the carbonatite melts solidify to a carbonatite rock that their former presence is clear, but that is not always the case. Often, carbonatite melts metasomatise and modify the rocks through which they flow, without forming a significant carbonate solid assemblage.[94] This process is often invoked for mantle metasomatism, and indeed some published apatite analyses report inexplicably low analytical totals, high silica, and no other component which might charge balance the silica.[95] We suggest that these mantle apatites might contain a significant carbonate component, implying the former presence of carbonate-bearing melts. Additionally, this demonstrates the potential of apatite to be a major CO_2 reservoir in the mantle.

Conclusions and outlook

Our data demonstrate the substitution $2PO_4^{3-} \rightarrow SiO_4^{4-} + CO_3^{2-}$ occurring on the tetrahedral site. We find that the structural position of carbonate is alternating between two positions which would otherwise be side faces of a phosphate tetrahedron. An oxygen vacancy is formed in the apex of the remaining tetrahedron. Despite analytical challenges, our synthesised apatite contains sufficient carbonate to account for this substitution.

Nonetheless, we experienced substantial difficulty in accurate apatite analysis using a variety of established and presumably trusted methods. Apatite is a prevalent material, ubiquitous in living organisms, the environment, and the deep Earth. Furthermore, apatite is an indispensable industrial material with applications in medicine and many other technologies. It is surprising that no established analysis protocol exists for such an important and widely studied material. We beseech the scientific community to put more attention on quantitative apatite analysis.

Author contributions

Michael Anenburg and Madeleine Humphreys conceived the study. Michael Anenburg performed the experiments and coordinated the project. Jeff Chen performed EPMA analyses and contributed to the carbon measurement method. Michael Gardiner performed the SCXRD measurement, with Owen Missen and Stuart Mills solving and refining the structure. Cees-Jan de Hoog conducted SIMS measurements and analysed the results with Madeleine Humphreys. Božana Pašić performed FTIR measurements. All authors significantly and heroically contributed to reconciling the contrasting analytical results.

Conflicts of interest

The authors declare no conflict of interest.

Data availability

Supplementary tables, raw instrumental data, and data processing routines written in the R scripting language are available at figshare: **https://doi.org/10.6084/m9.figshare.28398359**.

Acknowledgements

This project was supported by Australian Research Council (ARC) grants FL130100066, LP190100635, LP190100785, and IE240100103. The authors acknowledge Microscopy Australia (ROR: 042mm0k03) at the Centre for Advanced Microscopy, The Australian National University, a facility enabled by NCRIS and university support. MCSH acknowledges the support of the NERC ion microprobe facility (pilot grant IMFS114). MCSH was supported by the European Research Council (ERC) under the European Union's Horizon 2020 research and innovation programme (grant agreement No 864923). OPM acknowledges support from the project "Building capacity in Regional Australia to enhance Australia's Economy through research, training, and environmentally sustainable production of critical metals", supported by the Australian Government Department of Education. We thank ASA for drawing the watercolour table of contents entry.

References

1 Y. Jiang, Z. Yuan and J. Huang, *Mater. Technol.*, 2019, **35**, 785–796.
2 J. M. Hughes and J. Rakovan, *Rev. Mineral. Geochem.*, 2002, **48**, 1–12.
3 J. M. Hughes and J. F. Rakovan, *Elements*, 2015, **11**, 165–170.
4 Y. Pan and M. E. Fleet, *Rev. Mineral. Geochem.*, 2002, **48**, 13–49.
5 M. E. Fleet and X. Liu, *J. Solid State Chem.*, 2004, **177**, 3174–3182.
6 R. C. Tacker, *Am. Mineral.*, 2008, **93**, 168–176.
7 A. Aminian, M. Solati-Hashjin, A. Samadikuchaksaraei, F. Bakhshi, F. Gorjipour, A. Farzadi, F. Moztarzadeh and M. Schmücker, *Ceram. Int.*, 2011, **37**, 1219–1229.
8 I. R. Gibson, S. M. Best and W. Bonfield, *J. Biomed. Mater. Res.*, 1999, **44**, 422–428.
9 J. H. Lee, K. S. Lee, J. S. Chang, W. S. Cho, Y. Kim, S. R. Kim and Y. T. Kim, *Key Eng. Mater.*, 2003, **254–256**, 135–138; N. Patel, S. M. Best, W. Bonfield, I. R. Gibson, K. A. Hing, E. Damien and P. A. Revell, *J. Mater. Sci.: Mater. Med.*, 2002, **13**, 1199–1206; A. M. Pietak, J. W. Reid, M. J. Stott and M. Sayer, *Biomaterials*, 2007, **28**, 4023–4032; Z. Liu, L. Zhang, X. Wang, G. Jiang and M. Yang, *J. Mol. Model.*,

2018, **24**, 168; K. Asadipour, N. Nezafati, M. S. Nourbakhsh, M. Hafezi-Ardakani and S. Bohlooli, *Int. J. Artif. Organs*, 2019, **42**, 95–108.

10 A. E. Porter, N. Patel, J. N. Skepper, S. M. Best and W. Bonfield, *Biomaterials*, 2003, **24**, 4609–4620; A. E. Porter, C. M. Botelho, M. A. Lopes, J. D. Santos, S. M. Best and W. Bonfield, *J. Biomed. Mater. Res., Part A*, 2004, **69**, 670–679.

11 N. Hijon, M. Victoria Cabanas, J. Pena and M. Vallet-Regi, *Acta Biomater.*, 2006, **2**, 567–574.

12 M. Vallet-Regí and D. Arcos, *J. Mater. Chem.*, 2005, **15**, 1509–1516.

13 D. M. Ibrahim, A. A. Mostafa and S. I. Korowash, *Chem. Cent. J.*, 2011, **5**, 74.

14 J. H. Shepherd, D. V. Shepherd and S. M. Best, *J. Mater. Sci.: Mater. Med.*, 2012, **23**, 2335–2347.

15 E. Landi, J. Uggeri, S. Sprio, A. Tampieri and S. Guizzardi, *J. Biomed. Mater. Res., Part A*, 2010, **94**, 59–70.

16 L. T. Bang, S. Ramesh, J. Purbolaksono, Y. C. Ching, B. D. Long, H. Chandran, S. Ramesh and R. Othman, *Mater. Des.*, 2015, **87**, 788–796.

17 V. H. Hoang, M. A. Troubitsin, L. V. Furda and T. T. H. Nguyen, *J. Biomimetics, Biomater. Biomed. Eng.*, 2020, **47**, 1–12.

18 G. Spence, N. Patel, R. Brooks and N. Rushton, *J. Biomed. Mater. Res., Part A*, 2009, **90**, 217–224; G. Spence, N. Patel, R. Brooks, W. Bonfield and N. Rushton, *J. Biomed. Mater. Res., Part A*, 2010, **92**, 1292–1300; R. Yotsova and S. Peev, *Pharmaceutics*, 2024, **16**, 291; M. Safarzadeh, C. F. Chee and S. Ramesh, *Ceram. Int.*, 2022, **48**, 18174–18179; A. Cahyanto, M. Liemidia, E. Karlina, M. N. Zakaria, K. A. Shariff, C. Sukotjo and A. El-Ghannam, *Materials*, 2023, **16**, 2071.

19 Y. Tanizawa and T. Suzuki, *Phosphorus Res. Bull.*, 1994, **4**, 83–88.

20 L. Boyer, J. Carpena and J. L. Lacout, *Solid State Ionics*, 1997, **95**, 121–129.

21 D. S. Yoo, J. S. Cho, Y.-C. Chung and S.-H. Rhee, *J. Mater. Sci.*, 2021, **56**, 5493–5508.

22 I. Rehman and W. Bonfield, *J. Mater. Sci.: Mater. Med.*, 1997, **8**, 1–4.

23 F. M. McCubbin and R. H. Jones, *Elements*, 2015, **11**, 183–188; J. D. Webster and P. M. Piccoli, *Elements*, 2015, **11**, 177–182.

24 G. H. McClellan, *J. Geol. Soc.*, 1980, **137**, 675–681; A. C. Knudsen and M. E. Gunter, in Phosphates, ed. M. L. Kohn, J. Rakovan and J. M. Hughes, *Reviews in Mineralogy and Geochemistry*, vol. 48, ch. 363, 2002, pp. 363–389.

25 M. Anenburg, J. A. Mavrogenes and V. C. Bennett, *J. Petrol.*, 2020, **61**, egaa003.

26 G. M. Yaxley, M. Anenburg, S. Tappe, S. Decree and T. Guzmics, *Annu. Rev. Earth Planet. Sci.*, 2022, **50**, 261–293; H. Guo, J. Tuduri, Z. Nabyl, S. Erdmann, X. Li and F. Gaillard, *Earth Planet. Sci. Lett.*, 2024, **642**, 118863; G. Sartori, A. Galli, D. Weidendorfer and M. W. Schmidt, *Geology*, 2023, **51**, 54–58.

27 D. E. Harlov, *Elements*, 2015, **11**, 171–176.

28 J. Riker, M. C. S. Humphreys, R. A. Brooker, J. C. M. De Hoog and EIMF, *Am. Mineral.*, 2018, **103**, 260–270.

29 A. J. Ruys, *J. Australas. Ceram. Soc.*, 1993, **29**, 71–80.

30 B. Moreno-Perez, Z. Matamoros-Veloza, J. C. Rendon-Angeles, K. Yanagisawa, A. Onda, J. E. Pérez-Terrazas, E. E. Mejia-Martínez, O. Burciaga Díaz and M. Rodríguez-Reyes, *Bol. Soc. Esp. Ceram. Vidrio*, 2020, **59**, 50–64.

31 M. E. Fleet, X. Liu and P. L. King, *Am. Mineral.*, 2004, **89**, 1422–1432.

32 M. E. Fleet, *Front. Biosci.*, 2013, **5**, 643–652.

33 A. E. Patiño Douce, M. F. Roden, J. Chaumba, C. Fleisher and G. Yogodzinski, *Chem. Geol.*, 2011, **288**, 14–31.

34 F. E. Imrie, M. Corno, P. Ugliengo and I. R. Gibson, *Key Eng. Mater.*, 2012, **529–530**, 123–128; E. Bruand, M. Fowler, C. Storey and J. Darling, *Am. Mineral.*, 2017, **102**, 75–84; G. D. Bromiley, *Lithos*, 2021, **384–385**, 105900.

35 J. W. Reid, K. Fargo, J. A. Hendry and M. Sayer, *Mater. Lett.*, 2007, **61**, 3851–3854; V. Aina, G. Lusvardi, B. Annaz, I. R. Gibson, F. E. Imrie, G. Malavasi, L. Menabue, G. Cerrato and G. Martra, *J. Mater. Sci.: Mater. Med.*, 2012, **23**, 2867–2879; V. Aina, L. Bergandi, G. Lusvardi, G. Malavasi, F. E. Imrie, I. R. Gibson, G. Cerrato and D. Ghigo, *Mater. Sci. Eng. C*, 2013, **33**, 1132–1142; M. Kheradmandfard, M. H. Fathi, M. Ahangarian and E. M. Zahrani, *Ceram. Int.*, 2012, **38**, 169–175; E. Landi, A. Tampieri, M. Mattioli-Belmonte, G. Celotti, M. Sandri, A. Gigante, P. Fava and G. Biagini, *J. Eur. Ceram. Soc.*, 2006, **26**, 2593–2601; C. M. Botelho, R. A. Brooks, S. M. Best, M. A. Lopes, J. D. Santos, N. Rushton and W. Bonfield, *J. Biomed. Mater. Res., Part A*, 2006, **79**, 723–730; J. Kolmas, A. Jaklewicz, A. Zima, M. Bućko, Z. Paszkiewicz, J. Lis, A. Ślósarczyk and W. Kolodziejski, *J. Mol. Struct.*, 2011, **987**, 40–50; E. György, P. Toricelli, G. Socol, M. Iliescu, I. Mayer, I. N. Mihailescu, A. Bigi and J. Werckman, *J. Biomed. Mater. Res., Part A*, 2004, **71**, 353–358; Z. Huang, F. Cui, Q. Feng and X. Guo, *Ceram. Int.*, 2015, **41**, 8773–8778; D. J. Hickey, B. Ercan, L. Sun and T. J. Webster, *Acta Biomater.*, 2015, **14**, 175–184; Y. Cai, S. Zhang, X. Zeng, Y. Wang, M. Qian and W. Weng, *Thin Solid Films*, 2009, **517**, 5347–5351.

36 S. Sprio, A. Tampieri, E. Landi, M. Sandri, S. Martorana, G. Celotti and G. Logroscino, *Mater. Sci. Eng. C*, 2008, **28**, 179–187; N. Golafshan, M. Alehosseini, T. Ahmadi, A. Talebi, M. Fathi, M. Kharaziha, G. Orive, M. Castilho and A. Dolatshahi-Pirouz, *Mater. Sci. Eng. C*, 2021, **120**, 111611.

37 E. Landi, S. Sprio, M. Sandri, G. Celotti and A. Tampieri, *Acta Biomater.*, 2008, **4**, 656–663; A. Ressler, A. Žužić, I. Ivanišević, N. Kamboj and H. Ivanković, *Open Ceram.*, 2021, **6**, 100122.

38 A. C. Hack and J. A. Mavrogenes, *Am. Mineral.*, 2006, **91**, 203–210.

39 M. Anenburg and H. S. C. O'Neill, *J. Petrol.*, 2019, **60**, 1825–1832.

40 M. Cherdantseva, M. Anenburg, M. Fiorentini and J. Mavrogenes, *Sci. Adv.*, 2024, **10**, eadl3127.

41 J. Hammerli, J. Hermann, P. Tollan and F. Naab, *Contrib. Mineral. Petrol.*, 2021, **176**, 105.

42 R. C. Tacker, *Am. Mineral.*, 2004, **89**, 1411–1421.

43 L. Jeppsson, R. Anehus and D. Fredholm, *J. Paleontol.*, 1999, **73**, 964–972.

44 K. L. Wang, Y. Zhang and F. U. Naab, *Am. Mineral.*, 2011, **96**, 1392–1397.

45 K. Clark, Y. Zhang and F. U. Naab, *Am. Mineral.*, 2016, **101**, 2443–2451.

46 Y. Suetsugu and J. Tanaka, *J. Mater. Sci.: Mater. Med.*, 1999, **10**, 561–566.
47 M. Veiderma, K. Tõnsuaadu, R. Knubovets and M. Peld, *J. Organomet. Chem.*, 2005, **690**, 2638–2643; M. M. Bollmeyer, M. C. Carney and C. H. Yoder, *Am. Mineral.*, 2019, **104**, 438–446.
48 C. H. Yoder, M. M. Bollmeyer, K. R. Stepien and R. N. Dudrick, *Am. Mineral.*, 2019, **104**, 869–877.
49 C. H. Yoder and X. Lyu, *Polyhedron*, 2020, **179**, 114365.
50 J. C. J. Stormer, M. L. Pierson and R. C. Tacker, *Am. Mineral.*, 1993, **78**, 641–648; B. Goldoff, J. D. Webster and D. E. Harlov, *Am. Mineral.*, 2012, **97**, 1103–1115; M. J. Stock, M. C. S. Humphreys, V. C. Smith, R. D. Johnson, D. M. Pyle and EIMF, *Am. Mineral.*, 2015, **100**, 281–293.
51 J. D. Webster, C. M. Tappen and C. W. Mandeville, *Geochim. Cosmochim. Acta*, 2009, **73**, 559–581.
52 G. Schettler, M. Gottschalk and D. E. Harlov, *Am. Mineral.*, 2011, **96**, 138–152.
53 J. T. Armstrong, J. Donovan and P. Carpenter, *Microsc. Microanal.*, 2013, **19**, 812–813.
54 G. F. Bastin, J. M. Dijkstra and H. J. M. Heijligers, *X-Ray Spectrom.*, 1998, **27**, 3–10.
55 C. T. Chantler, K. Olsen, R. A. Dragoset, J. Chang, A. R. Kishore, S. A. Kotochigova and D. S. Zucker, X-Ray Form Factor, Attenuation and Scattering Tables (version 2.1). [Online] Available: **http://physics.nist.gov/ffast** [2025-07-10]. National Institute of Standards and Technology, Gaithersburg, MD, 2005.
56 M. J. Stock, M. C. S. Humphreys, V. C. Smith, R. Isaia, R. A. Brooker and D. M. Pyle, *J. Petrol.*, 2018, **59**, 2463–2492.
57 N. Shimizu and S. R. Hart, *Annu. Rev. Earth Planet. Sci.*, 1982, **10**, 483–526.
58 J. Cosier and A. M. Glazer, *J. Appl. Crystallogr.*, 1986, **19**, 105–107.
59 *Agilent, CrysAlis PRO*, Agilent Technologies Ltd, Yarnton, Oxfordshire, England, 2014.
60 G. M. Sheldrick, *Acta Crystallogr., Sect. A: Found. Adv.*, 2015, **71**, 3–8.
61 G. M. Sheldrick, *Acta Crystallogr., Sect. C: Struct, Chem.*, 2015, **71**, 3–8.
62 C. B. Hubschle, G. M. Sheldrick and B. Dittrich, *J. Appl. Crystallogr.*, 2011, **44**, 1281–1284.
63 O. C. Gagné and F. C. Hawthorne, *Acta Crystallogr., Sect. B: Struct. Sci., Cryst. Eng. Mater.*, 2015, **71**, 562–578.
64 N. E. Brese and M. O'Keeffe, *Acta Crystallogr., Sect. B: Struct. Sci.*, 1991, **47**, 192–197.
65 J. Sommerauer and K. Katz-Lehnert, *Contrib. Mineral. Petrol.*, 1985, **91**, 360–368.
66 M. E. Fleet, X. Liu and X. Liu, *Am. Mineral.*, 2011, **96**, 1148–1157.
67 Y. Suetsugu, Y. Takahashi, F. P. Okamura and J. Tanaka, *J. Solid State Chem.*, 2000, **155**, 292–297.
68 M. Anenburg, T. L. Panikorovskii, E. S. Jennings, R. Y. Shendrik, A. A. Antonov and V. Gavrilenko, *Inorg. Chem.*, 2024, **63**, 11788–11801.
69 Y. Su, F. S. Brigiano, I. Petit, C. Leroy, C. Bonhomme, F. Babonneau, F. Tielens and C. Gervais, *ChemistryMethods*, 2023, **3**, e202300007.
70 M. E. Fleet and X. Liu, *Biomaterials*, 2007, **28**, 916–926.
71 B. Buse and S. Kearns, *Microsc. Microanal.*, 2015, **21**, 594–605.
72 J. Berndt and S. Klemme, *Nat. Commun.*, 2022, **13**, 2892.
73 I. M. Kulikova, O. A. Nabelkin, V. A. Ivanov and I. A. Filenko, *Phys. Solid State*, 2021, **63**, 1695–1703; G. F. Bastin and H. J. M. Heijligers, *X-Ray Spectrom.*, 1986, **15**, 135–141.
74 X. Zhang, S. Yang, H. Zhao, S. Jiang, R. Zhang and J. Xie, *J. Earth Sci.*, 2018, **30**, 834–842.
75 R. A. Ketcham, *Am. Mineral.*, 2015, **100**, 1620–1623.
76 N. Y. Mostafa, H. M. Hassan and O. H. Abd Elkader, *J. Am. Ceram. Soc.*, 2011, **94**, 1584–1590.
77 M. Palard, E. Champion and S. Foucaud, *J. Solid State Chem.*, 2008, **181**, 1950–1960.
78 S. Gomes, J.-M. Nedelec, E. Jallot, D. Sheptyakov and G. Renaudin, *Cryst. Growth Des.*, 2011, **11**, 4017–4026.
79 L. T. Bang, B. D. Long and R. Othman, *Sci. World J.*, 2014, **2014**, 969876.
80 Y. Banno, R. Miyawaki, K. Momma and M. Bunno, *Mineral. Mag.*, 2016, **80**, 363–370.
81 D. U. Schramm, J. Terra, A. M. Rossi and D. E. Ellis, *Phys. Rev. B: Condens. Matter Mater. Phys.*, 2000, **63**, 024107.
82 S. Klemme, *J. Mineral. Petrol. Sci.*, 2010, **105**, 1–8.
83 Z. Zyman and M. Tkachenko, *J. Eur. Ceram. Soc.*, 2011, **31**, 241–248.
84 J. W. Reid, A. Pietak, M. Sayer, D. Dunfield and T. J. Smith, *Biomaterials*, 2005, **26**, 2887–2897.
85 R. Astala, L. Calderín, X. Yin and M. J. Stott, *Chem. Mater.*, 2005, **18**, 413–422.
86 K. S. Leshkivich and E. A. Monroe, *J. Mater. Sci.*, 1993, **28**, 9–14.
87 M. Safarzadeh, S. Ramesh, C. Y. Tan, H. Chandran, A. F. M. Noor, S. Krishnasamy, U. J. Alengaram and S. Ramesh, *Ceram. Int.*, 2019, **45**, 3473–3477.
88 C. H. Yoder, K. R. Stepien and T. M. Edner, *J. Therm. Anal. Calorim.*, 2020, **140**, 2179–2184.
89 T. Leventouri, *Biomaterials*, 2003, **24**, 4205–4211; D. Arcos, J. Rodríguez-Carvajal and M. Vallet-Regí, *Chem. Mater.*, 2004, **16**, 2300–2308.
90 N. Y. Mostafa, H. M. Hassan and F. H. Mohamed, *J. Alloys Compd.*, 2009, **479**, 692–698.
91 A. Antonakos, E. Liarokapis and T. Leventouri, *Biomaterials*, 2007, **28**, 3043–3054.
92 R. C. Tacker and J. C. J. Stormer, *Am. Mineral.*, 1989, **74**, 877–888; H. Li and J. Hermann, *Geochim. Cosmochim. Acta*, 2015, **166**, 267–297; H. Li and J. Hermann, *Chem. Geol.*, 2017, **473**, 55–73; H. Li and J. Hermann, *Am. Mineral.*, 2017, **102**, 580–594; W. Li and F. Costa, *Geochim. Cosmochim. Acta*, 2020, **269**, 203–222; M. C. S. Humphreys, V. C. Smith, J. P. Coumans, J. M. Riker, M. J. Stock, J. C. M. de Hoog and R. A. Brooker, *Earth Planet. Sci. Lett.*, 2021, **576**, 117198; C. L. Nathwani, S. J. E. Large, E. R. Brugge, J. J. Wilkinson and Y. Buret, *Contrib. Mineral. Petrol.*, 2023, **178**, 49.
93 M. Anenburg and I. N. Aslam, *Volcanica*, 2024, **7**, 813–833; A. G. Christy, I. V. Pekov and S. V. Krivovichev, *Elements*, 2021, **17**, 333–338.
94 T. Guzmics, Z. Zajacz, J. Kodolányi, W. Halter and C. Szabó, *Geochim. Cosmochim. Acta*, 2008, **72**, 1864–1886; S. Y. Wass, P. Henderson and C. J. Elliott, *Philos. Trans. R. Soc. London, Ser. A Philos. Trans.: Math., Phys. Eng. Sci.*, 1997, **297**, 333–346.
95 G. M. Yaxley and V. Kamenetsky, *Earth Planet. Sci. Lett.*, 1999, **172**, 97–109.

